Available online at www.sciencedirect.com

SCIENCE DIRECT®

Experimental Thermal and Fluid Science 30 (2005) 117–130

Experimental Thermal and Fluid Science

www.elsevier.com/locate/etfs

Measurements of droplets characteristics in a swirl-stabilized spray flame

R. Hadef [a,*], B. Lenze [b]

[a] *Institut de Génie Mécanique, Université Larbi Ben M'Hidi, BP 297, 04000 Oum El Bouaghi, Algeria*
[b] *Engler-Bunte-Institut, Chair of Combustion Technology, University of Karlsruhe, Germany*

Received 12 August 2004; accepted 2 May 2005

Abstract

Experiments have been performed in a kerosene airblast atomized spray flame where the fuel supply is sandwiched between two coswirling air streams. A phase-Doppler particle sizing system was used to measure fuel droplet size, velocity and turbulent kinetic energy of droplets and gas as well as the fuel volume flux within the combustor for two values of air preheat temperature, 200 °C and 400 °C. The results reveal that a small liquid fuel exists in the centre of the combustor and due to larger droplets with the swirl effect; the droplets characteristics (velocity and turbulent kinetic energy) did not follow the gas ones. Based upon these measurements, an optimum swirl number will exist with every atomization and burner arrangement of a liquid-fuelled flame associated and will be different from that associated with the corresponding gas-fuelled flame. The investigated atomizer shows a marked influence of the inlet air temperature on the measured droplet size which may be attributed to the design of the internal airflow, promoting prompt atomization at the dominant atomization mode.

Keywords: Spray flame; Swirl; Airblast; Phase-Doppler anemometry

1. Introduction

The combustion of liquid fuels currently provides the energy used by a variety of power systems such as industrial furnaces and boilers, as well as automotive and aerospace engines. The performance of a given spray combustion system depends not only on the fuel droplet size distribution but on the spray spatial distribution and the interaction of the droplets with the gas turbulence that involves a physical mechanism that it is not well understood [1]. For this reason, spatially- and temporally-resolved information (i.e. the mean and root-mean-square velocities of both phases, the mean droplet size and droplet size distribution as well as the droplet mass flux) needs to be determined in order to understand the most favourable spray conditions for optimal performance of the appliances. Up to now, no techniques came closer to obtain these data than laser-based diagnostic methods, which share the common advantage of being inherently non-intrusive and in situ, and can be made with high temporal and spatial resolution.

In this work, an experimental investigation is carried out using the phase-Doppler anemometry (PDA) [2] in order to measure the characteristics of the fuel droplets interacting with the flow/flame in a typical turbine combustor. The stabilized kerosene flame is formed by a coswirling double annular flow and a prefilming airblast atomizer [3], which is used because of its advantages such as a low fuel pressure requirement, a large flow turndown ratio and low pollutant emissions. Earlier experimental investigations [4–7] have revealed that the swirling air streams apart from enhancing mixing,

---

[*] Corresponding author. Tel.: +213 32 48 63 74; fax: +213 32 49 29 98.

E-mail address: rhadef@rocketmail.com (R. Hadef).

0894-1777/$ - see front matter © 2005 Elsevier Inc. All rights reserved.
doi:10.1016/j.expthermflusci.2005.05.002

Nomenclature

AFR	air-to-fuel mass flow rate ratio (–)
A_z	reference area (m^2)
b	function in the PDA system (–)
C, C'	efficiencies of the atomization process
C_μ	constant in the expression of μ_{turb}
d	droplet diameter (m)
d_0	initial droplet diameter (m)
d_{b}	droplet diameter before a break-up (m)
d_i	diameter of the *i*-droplet (m)
d_{p}	particle diameter (m)
D	combustor diameter (m)
D_{b}	diameter of the atomizer throat (m)
$F_{\mathrm{L}z}$	liquid flux in the *z*-direction ($\mathrm{m}^3/\mathrm{m}^2\,\mathrm{s}$)
F_{D}	frequency of Doppler burst (s^{-1})
k	turbulent kinetic energy ($\mathrm{m}^2/\mathrm{s}^2$)
K	constant of evaporation (m^2/s)
l_{turb}	turbulence length scale (m)
l_{min}	minimum length of the probe volume (m)
$\dot{m}_{\mathrm{A}}$	atomizing air mass flow rate (kg/h)
$\dot{m}_{\mathrm{L}}$	liquid-fuel mass flow rate (kg/h)
n	number of validated droplets (–)
r	radial coordinate (m)
$S_{0,\mathrm{th}}$	theoretical swirl number (–)
S_{in}	inner swirl number (–)
S_{ou}	outer swirl number (–)
St_{swirl}	swirl Stokes number (–)
St_{turb}	turbulence Stokes number (–)
SMD	Sauter mean diameter (–)
SMD_0	initial Sauter mean diameter (–)

t	time (s)
t_{L}	thickness of the liquid film (m)
T_0	air preheat temperature (°C)
Δt_{s}	sampling time (s)
Δt_{1-2}	time difference between two-burst signals (s)
U	mean axial velocity component (m/s)
U_{A}	atomizing air velocity (m/s)
U_{L}	liquid-fuel velocity (m/s)
$U_\perp$	particle velocity normal to the fringes (m/s)
V	mean radial velocity component (m/s)
W	mean tangential velocity component (m/s)
z	axial coordinate (m)

Greek letters

ε	dissipation rate of k ($\mathrm{m}^2/\mathrm{s}^3$)
γ_i	particle trajectory angle
λ	wavelength of the laser beam (m)
μ	dynamic viscosity of the gas (kg/m s)
μ_{turb}	turbulent viscosity (kg/(m s)), $\rho_A C_\mu k^2/\varepsilon$
θ	intersection angle between the laser beams (rad)
ρ_{A}	air density ($\mathrm{kg/m}^3$)
ρ_{L}	liquid-fuel density ($\mathrm{kg/m}^3$)
σ	liquid-fuel surface tension (N/m)
τ_{relax}	droplet relaxation time, $\rho_{\mathrm{L}} d^2/18\mu$ (s)
τ_{swirl}	swirl characteristic time of the gas flow, ω^{-1} (s)
τ_{turb}	turbulence time scale of the airflow (s)
ω	angular velocity of gas (rad/s)
$\Delta\varphi_{1-2}$	phase shift between two-burst signals (rad)

increasing combustion efficiency and controlling emission of pollutants from the combustion, also promote the disintegration of the liquid sheet. On the other hand, this double concentric burner allows for variation of the radial distribution of swirl via control over the axial and angular momentum of the jets in the two annuli of the burner. As such, at a fixed overall swirl number, the detailed flow distribution can be significantly different under various operational conditions of the burner. By introducing the swirling flow through concentric annuli, it is possible to control the radial distribution of flow and swirl for achieving significantly different flame stability limits, levels of turbulence, volumetric heat release rates, and combustion characteristics in general [8–10].

The combustor configuration selected for this study is of practical interest since it is typical of industrial devices and is a compromise between the complexity of a real situation and a simplified laboratory model. In addition, the influence of the higher inlet air temperature on the spray characteristics and evaporation has been studied by measuring an additional complete data set for the same mixture in the present geometry.

2. Experimental arrangement

2.1. Atomizer

The swirl-stabilized combustor employed was a model laboratory complex flow combustor developed in a series of tests. The air stream was electrically preheated up to 400 °C and split equitably between an inner channel and an outer annular passage. The fuel was pressurized to 8 bar and delivered to the injector. The spray liquid sheet was injected from the fuel nozzle, which induces a low swirl due to its shape and first encounters the swirling inner airflow. This latter makes the liquid sheet unstable and disintegrates it into ligaments and droplets. The smaller droplets follow the flow, but the larger ones and fragments of the sheet attach to the prefilming surface forming a thin wavy film, and interfacing the inner swirling air. Upon arriving at the prefilmer lip, the film separates and is then exposed to high-speed swirling air streams on both sides. The liquid sheet–air interaction generally produces waves that become unstable and disintegrate into fragments. These fragments become ligaments and, in turn, break down into droplets. The review of several investigations carried out [11] reported that the important parameters influencing the atomization of low viscosity liquids (such as kerosene) are the initial thickness of liquid sheet and the air momentum. The interaction between the oxidizer flow field and droplets is very complex including turbulent heat, mass and momentum transfer as well as complicated chemical kinetics. Each of these phenomena is extremely complicated in its own right, and when coupled together in a real flow situation, forms a formidable challenge for the combustion research.

2.2. Optical diagnostic

The PDA technique was used for droplet sizing and velocity measurement. This technique determines the droplet velocity by standard fringe mode laser anemometry, and establishes the droplet size by measuring the phase shift of light encoded in the spatial variation of the fringes reaching two detectors after traveling paths of different lengths through the droplets (Fig. 1a). The phase shift is measured by two detectors, each looking at a spatially distinct portion of the collection lens. The frequency of the Doppler burst is directly proportional to the droplet velocity component perpendicular to the plane of fringes and the measured phase shift is related linearly to the droplet diameter by a so-called phase factor, which is determined by the geometry of the optical arrangement of the PDA system, the wavelength of the laser light, and the mechanism of light scattering (reflection or refraction). To eliminate the ambiguity associated with spatial phase shifts of over 360°, an additional detector may be added. The technique is insensitive to the amplitude of the scattered light and provides additional local point information including liquid flux, drop number density and size–velocity correlation. The theory of operation of a PDA system is well-established [12] and therefore will not be repeated here.

The specific instrument employed here was a two-colour dual-mode PDA [13]. As shown in Fig. 1b, it combines a standard two-detector PDA (SPDA) arrangement on one colour and a planar two-detector PDA (PPDA) one on another colour in a single appropriate optical receiving probe. In the first configuration, the detectors were located outside of the plane defined by the incident laser beams; conversely, in the second one the detectors were located in the same plane as the incident beams. This design was developed to improve measurement accuracy of liquid volume flux [14].

The size measurement was performed using the phase difference measured with the standard PDA due to its higher resolution; the planar PDA is used to resolve the 2π-ambiguity. The validation criterion consists of comparing the droplet diameter measured by the PPDA (equatorial line) with the droplet diameter measured by the SPDA (meridian line) to determine whether the

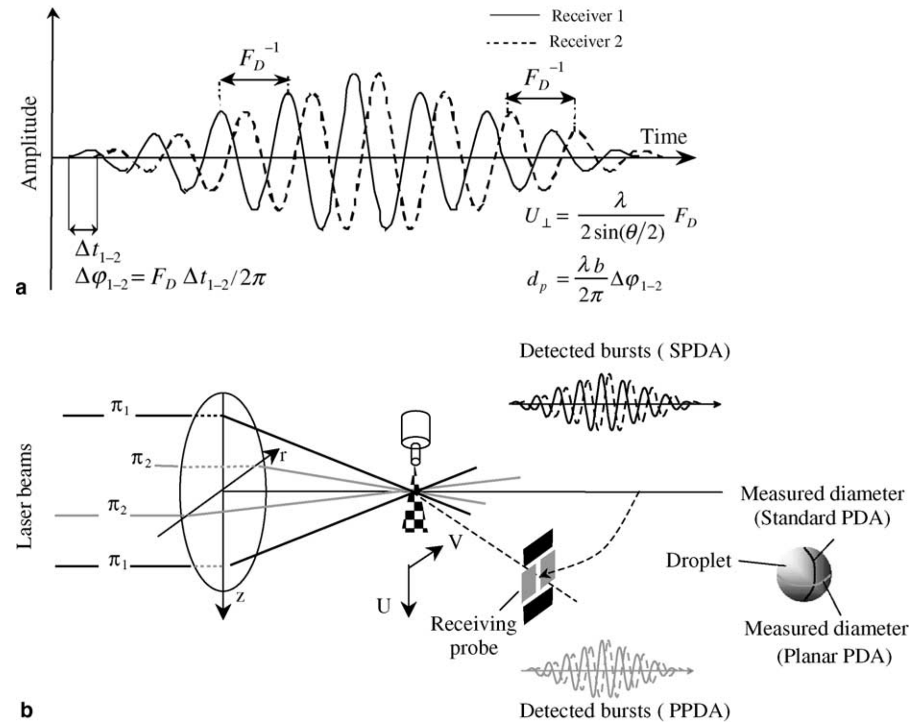

Fig. 1. (a) Band-pass filtered Doppler burst signals illustrating the phase shift between two detectors and (b) optical arrangement of a dual-mode phase-Doppler system.

measurement will be accepted or discarded. As both PDA configurations are affected in a different sense by the trajectory effect [15], the slit effect [16] and non-spherical droplet [17], this validation procedure provides an effective means to identify and reject erroneous measurements. The validation routine also includes a step which rejects signals when droplets have not crossed a minimum length of the measurement, $l_{\min}$, which is a specified percentage of the nominal measurement volume diameter. This validation step is necessary in connection with the determination of the effective measurement volume size. Another advantage of the dual-mode PDA system is that since it inherently measures two velocity components, the liquid volume flux vectors can be computed for each vector component. Its measure is based on the count of the number and size of droplets passing through a reference area, $A(d_i, \gamma_i)$ per unit time as given in the equation below for the component of the volume in the z-direction (main direction of the flow):

$$f_{v,z} = \frac{\pi}{6\Delta t_{\mathrm{s}}} \sum_{i=1}^{n} \frac{d_i^3}{A_z(d_i, \gamma_i)} \cos \gamma_i \tag{1}$$

where n denotes the total number of detected and validated droplets, and d_i and γ_i are the diameter and the trajectory of the ith droplet. The droplet size dependent cross-section of the measurement volume $A_z(d_i, \gamma_i)$ is calculated by the so-called burst length method [18], which is modified slightly to yield more accurate results in size classes with few droplets and to account better for particle trajectories [13].

2.3. Operating conditions

The combustor was operated at atmospheric pressure with a kerosene flow rate of 2.5 kg/h, corresponding to a thermal power load of 30 kW. A total air flow rate of 73.50 kg/h was distributed equally between both streams, resulting in an overall equivalence ratio of approximately 0.5. The Reynolds numbers of the flow, based on the hydraulic diameter, were 33,300 and 24,980 for inner and annular airflows, respectively. Theoretical swirl numbers ($S_{0,\mathrm{th}}$) of both inner and outer airflows (S_{in} and S_{ou}) were calculated using only geometrical data of the radial swirl generator [19] such as the ratio of tangential to axial momentum flux divided by the diameter of the burner throat, $D_{\mathrm{b}} = 25$ mm. According to this, the swirl numbers are 0.46 and 1.0 in the inner and outer flows, respectively. However, since the droplets absorb both angular and axial momentum from the airflow in the process of atomization, the resulting airflow swirl numbers can be slightly modified.

The flow control system for the burner consisted of a series of rotameters, pressure gauges, and control valves to measure and regulate the airflow rates prior to their entry into the two annuli and fuel flow rate into the nozzle of the burner. The spray was ignited by a high voltage spark and the flame was confined in a 10-cm internal diameter cylindrical combustion chamber. Limitation of the main reaction zone was provided by an orifice with 40% diameter reduction placed at the exit of the combustion chamber. Two plain quartz windows were mounted to provide the desired optical access into the combustion chamber. The entire burner was fixed and the optical setup was mounted on a three-axis stepper motor traverse system.

The light source was a multi-line argon ion water-cooled laser (Coherent Innova 70) operating at 488 nm and 514.5 nm with approximately output power of 200 mW. In the fibre drive unit, the laser light was colour separated (514.5 nm for the axial component, 488 nm for the radial or tangential component) and the two beams split into four and coupled into monomode glass fibres, which conducted them to the transmitting optics unit. One beam of each colour was frequency shifted by 40 MHz through a Bragg cell for the purpose of direction recognition of the velocities. The polarisation direction was adjusted perpendicular to the scattering plane. The transmitter aligned and focused the four beams to form the probe volume, which was around 53 μm in diameter and 2 mm in length. The scattering light is collected by a receiving lens with a focal length of 400 mm, which is placed at a 30° off-axis forward scatter mode, where the scattering of light by refraction is in the dominant mode and yields a linear relation of particle size and phase between the photodetectors over the detectable size range of the instrument. After colour separation by filters, the light fell onto the detectors regions where it was coupled again into glass fibres to reach the photomultipliers and transformed into electrical signals. The signals were processed by a covariance-processor of the PDA system. With this processor, the frequency and the phase shift of the filtered and amplified signals are determined. The signals are processed if the signal to noise of the every burst of a droplet is −3 dB or better. The measuring error for the mean and the r.m.s. velocity is about 1% and 3%, respectively. The uncertainty of the droplets size measurements is about ±5%, which is the aggregate error due to possible optical misalignment, changes of droplet refractive index during heat-up, and photomultiplier voltage setting. The uncertainty of the liquid volume flux is about 15% due to the Gaussian beam effect, the spherical validation and the calculation of the cross-sectional area [20].

3. Results

In the following section, the experimental results for the air preheated temperature of 200 °C are discussed in more detail. The measurements include velocity components, turbulent kinetic energy of both phases, droplet size, droplet number density and the liquid volume flux. For each measurement location, 5000 samples are recorded to allow a determination of the mean properties with low statically error. No measurement was made when the data rate was below 5 Hz. In addition, measurements below an axial height of 11 mm were not possible, due to optical access restrictions.

3.1. Flame form

Fig. 2a presents a time-exposure direct photograph of the investigated flame. It shows the stabilized inverted conical flame detached from the front wall, and slightly lifted from the nozzle mouth. By stabilizing a detached flame, a gap between the atomizer and the flame front occurs. In this gap the fuel is prevaporized and premixed and so a lean homogeneous combustion can be obtained without a premix duct.

Fig. 2b shows pseudo-streamlines on the *z*–*r* plane based on the mean axial and radial velocity components for a stable flame. The overall structure of the gas flow field can be mainly divided into three regions: a central toroidal recirculation zone (CTRZ), caused by the adverse pressure gradient induced by the swirl, a corner recirculation zone (CRZ), due to the air stream radial expansion and the wall confinement; and a dual shear layer (inner layer around the CTRZ and the outer layer around the CTZ). Both recirculation zones entrain smaller droplets and hot chemically active combustion species from the downstream region of the flame to the root of this one to improve flame stability. In general, the lowest mean temperature occurs in the CRZ because of the cooling wall effect and the highest temperature fluctuations occur in the shear mixing region where gradients are large.

3.2. Droplet size

An effective method of expressing the quality of atomization is the mean diameter. Probably, the most common form of mean droplet size is the Sauter mean diameter (SMD), which has the physical interpretation as the diameter of a droplet whose ratio of volume to surface area is the same as that of the entire spray. The variation of the SMD at several axial and radial stations is presented in Fig. 3. In all given measurements planes the smallest droplets are found in the vicinity of the wake of the atomizer lip. Because of their high inertia, only large droplets are able to penetrate the region of hot recirculating combustion gases, so that a relative concentration of droplets with $20\ \mu\text{m} < \text{SMD} < 70\ \mu\text{m}$ within the radial range from $0 < r < 10$ mm at $z = 11$ mm is observed. In the CTRZ with increasing the distance from the inlet, SMD shows a quick decrease due to the fast evaporation of the droplets. Due to the swirling motion of the gas flow and to resulting centrifugal forces, larger droplets are separated from the smaller ones and cause an increase in droplet size at higher radii. Because of their small surface to volume ratio, large droplets evaporate later, resulting in a less dependence of SMD on local measurement position with increasing distance from the atomizer.

A further analysis of these measurements data concerns the probability density function (pdf) of the droplet size and velocity components and reveals that all pdfs exhibit monomodal shapes. An example of the droplet diameter distribution at distance $z = 11$ mm from the nozzle is shown for three radial locations in Fig. 4a. For $r = 4$ mm, i.e. at a position quite close to the nozzle, the date rate is low and the distribution is more narrow since 90% of the droplets have a

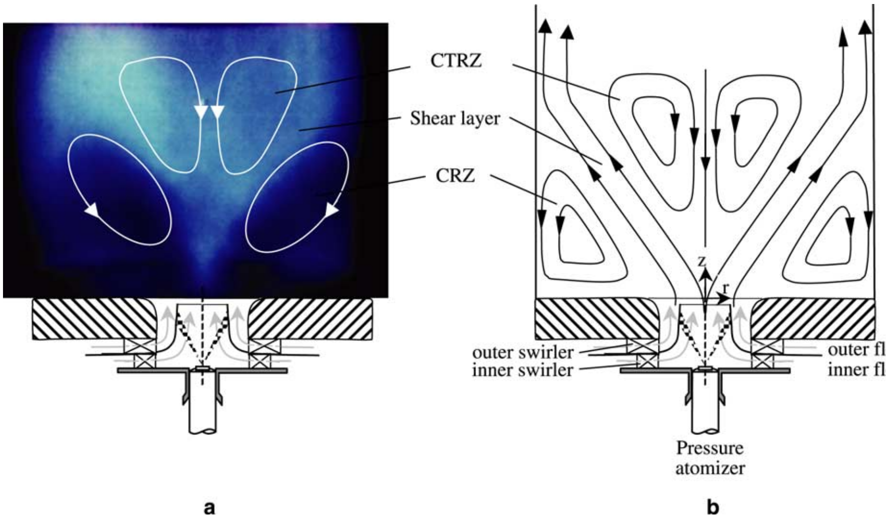

Fig. 2. (a) Photograph of the flame spray and (b) qualitative schematic of the gas flow field inside the combustion chamber.

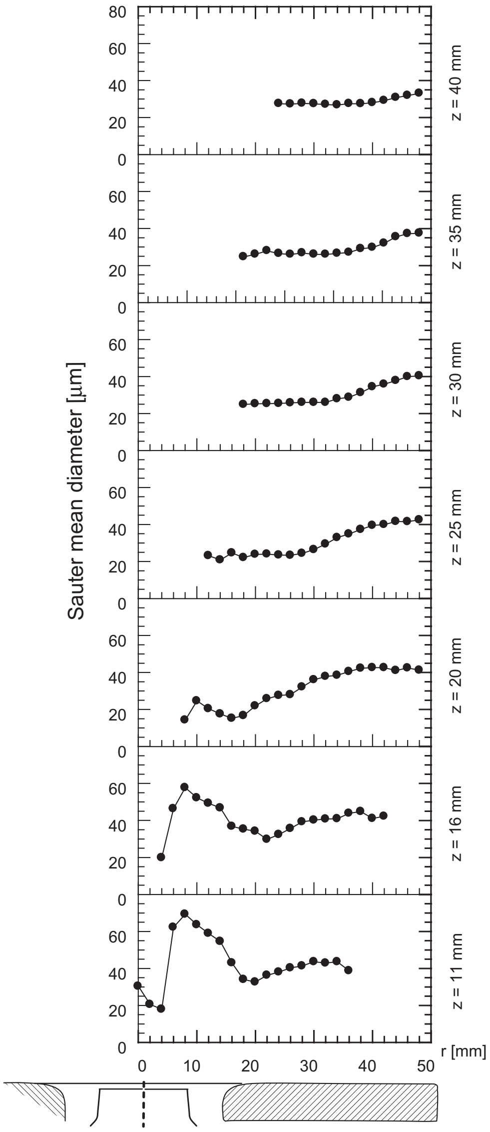

Fig. 3. SMD radial profiles at various axial locations.

diameter lower than 9 µm. Close to the shear layer ($r = 20$ mm), the spray is very dense and due to the presence of various droplet sizes the distribution becomes rather wide and displays a discrete maximum. For $r = 32$ mm, i.e. at a position close to the outside of the spray, the date rate is very low and the distribution is more broad, showing a large variation in droplet size and a broad maximum ranging from 18 to 35 µm which represents almost half of the population. Fig. 4b presents the variation of the SMD with the size of the considered droplets. It reveals that, despite of the weak presence of the large droplets, the latter influence considerably the measured value of SMD. However, this effect is non-existent for the value of the turbulent kinetic energy (Fig. 4c) because these large particles have a low value of the pdf(d_i) and the turbulent kinetic energy, k_i, simultaneously.

3.3. Drop number density and volume liquid flux

The fuel droplet number density is an important parameter for characterizing and understanding the collective behaviour of droplets in spray. The effects of drop acceleration/deceleration and collision can also be evaluated based upon number density distribution information. The distribution variation of this quantity is shown in Fig. 5a. At the inlet of the combustion chamber, the radial profile is characterized two peaks which indicate that few (larger) droplets coming from the inlet are still present in the boundaries of the CRTZ, while at the same time more droplets are entrained into the shear layer of the CRZ and disappear. As downstream distance increases, the droplet number density generally exhibits a gradual increase with radial distance to reach a peak, followed by a decrease to zero at the spray boundary. When traversing further downstream, the fuel droplet number density is found to be decreasing because of the spreading of the jet, as well as the droplet vaporization and eventual disappearance.

The liquid flux provides the criteria for the evaluation of the evaporation and the mixing rate in the spray. Local fuel/air mixture ratio determines the effectiveness of the spray combustion. The data are obtained via the validated drop size measurements in the probe volume during the entire sampling period. The radial profiles of the axial liquid flux shown in Fig. 5b are found to be similar to those of the droplet number density and the spray is spreading according to the cone of 84°. Note that inside the CTRZ, though the SMD profiles indicate the presence of droplets, the latter are in such small numbers, which evaporate rapidly (small droplets in the higher temperature region), that the liquid flux is negligible. Globally, the liquid flux is positive in all regions but it has been measured negative (with very small values) for both droplets class sizes, 0–4.5 µm and 4.5–9 µm, in the centre of the CTRZ and near the wall as it has been shown in Fig. 6.

These results point out that this configuration subjects the fuel spray to a large injection angle, causing a void of droplet concentration in the CTRZ. Far downstream, the liquid flux is distributed more uniformly over the whole cross-section of the spray since mean droplet sizes and droplet velocities become more uniform. However, the internal recirculation zone is not evident in the liquid volume flux profiles. This is because the larger droplets with axial velocity (positive) higher than the mean value of all droplets (negative), do not reverse their direction and result in a positive total axial liquid volume flux (Table 1).

3.4. Gas and drop velocities

One parameter that is of utmost importance for combustion spray modelling is the velocity of droplets, since

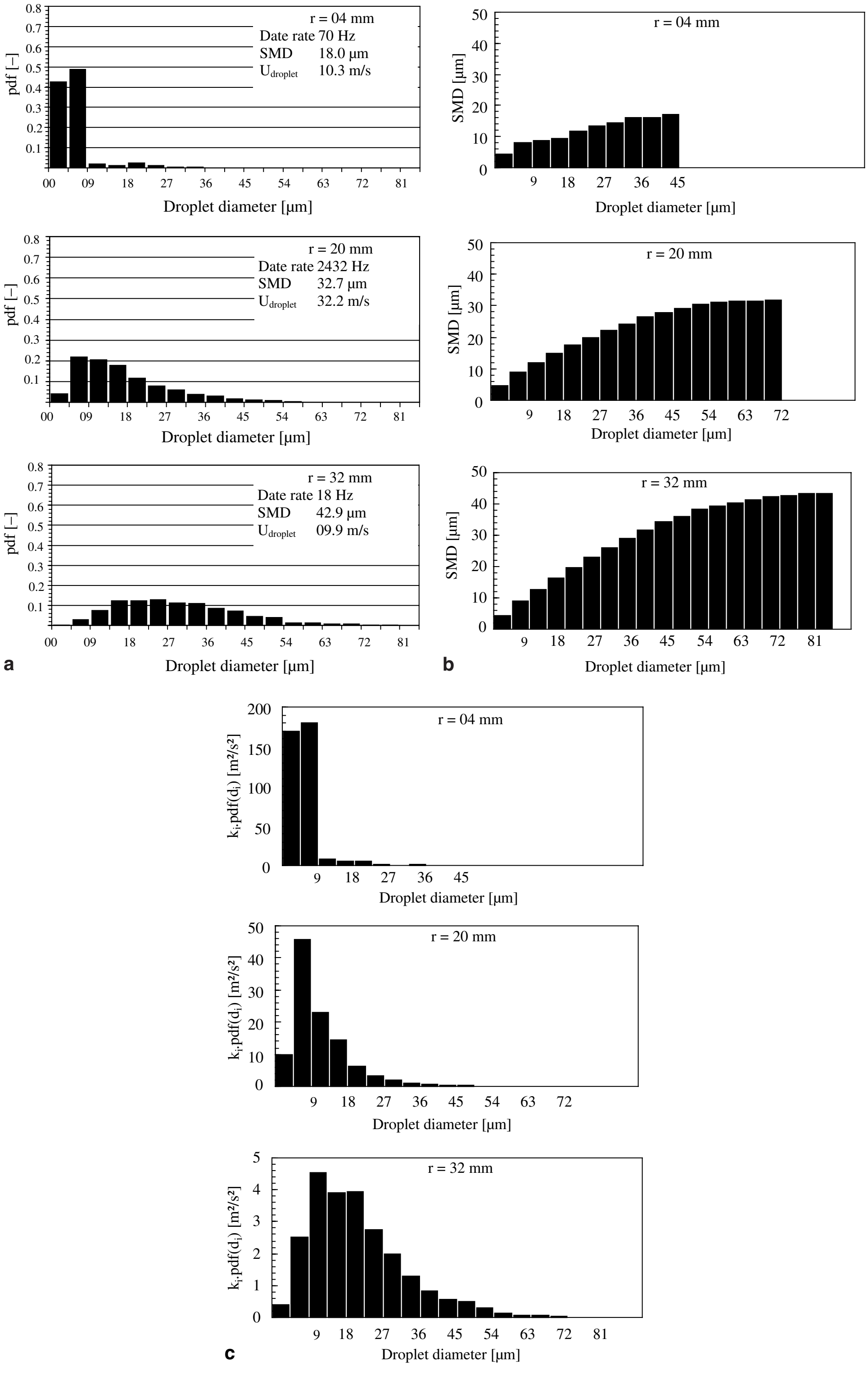

Fig. 4. (a) Distribution of droplets size at $z = 11$ mm, (b) variation of SMD with the droplet size class at $z = 11$ mm, and (c) distribution of droplets turbulent kinetic energy at $z = 11$ mm.

drag coefficients and trajectory angles can be determined from this information. Because of the complex interaction between the dispersed and gas phases, velocity and trajectory angle are difficult to model. It is useful, then, to display these characteristics for this selected burner.

The fidelity with which a droplet is able to follow the swirling gas flow is quantified in terms of the swirl

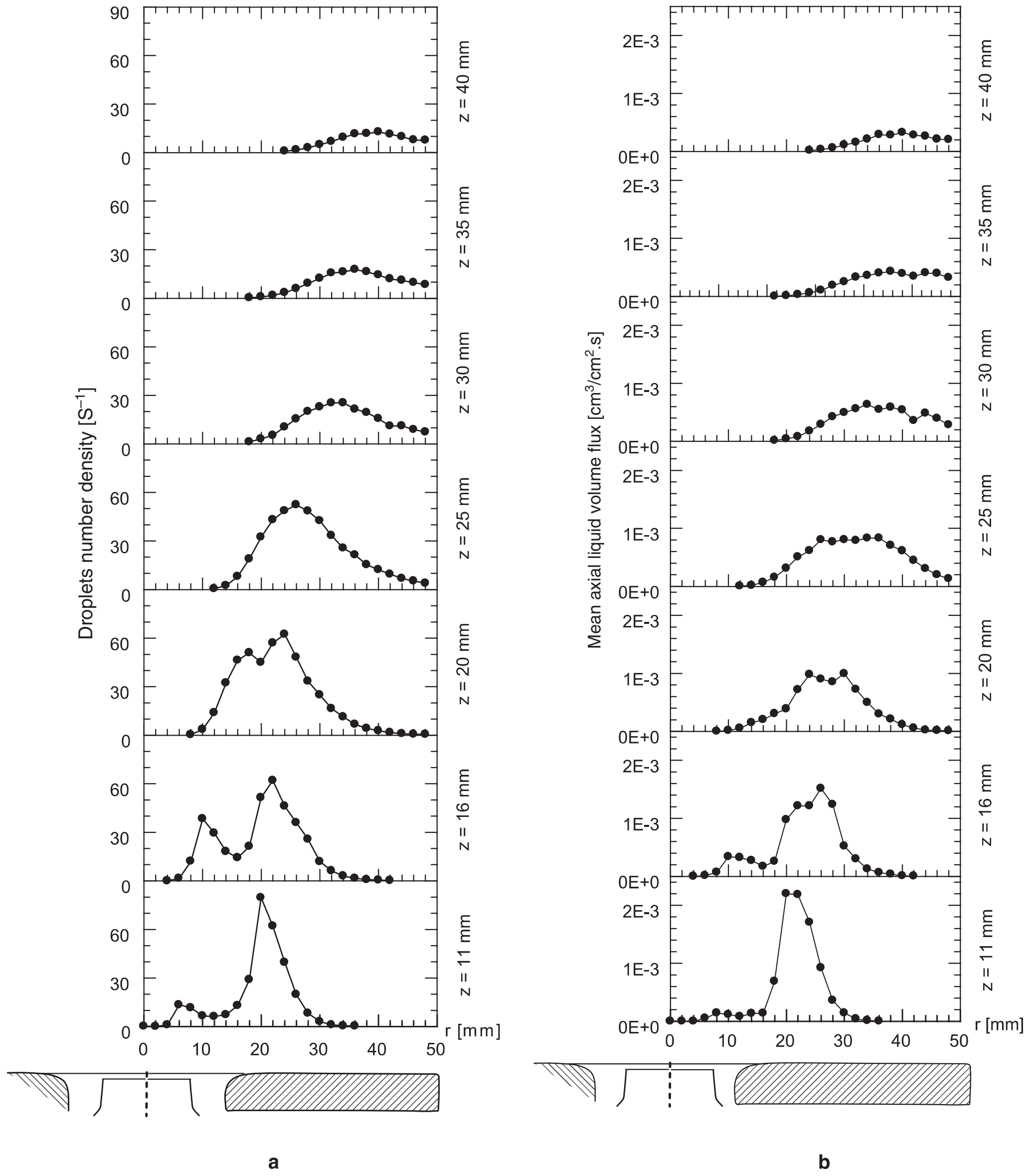

Fig. 5. (a) Droplets number density radial profiles at various axial stations and (b) axial liquid volume flux radial profiles at various axial stations.

Stokes number, St_{swirl}, which is defined as the ratio of the droplet relaxation time τ_{relax} to the swirl characteristic time of the airflow τ_{swirl} [21]:

$$St_{\text{swirl}} = \frac{\tau_{\text{relax}}}{\tau_{\text{swirl}}} \tag{2}$$

Its value indicates whether droplet movement in the swirling airflow is dominated by centrifugal forces, resulting in radial displacement of the droplet, or whether it is dominated by the drag force, causing the droplet to follow the streamlines of the airflow faithfully. The latter case is expected for $St_{\text{swirl}} < 0.1$, in which case the droplet is able to closely follow the curved fluid stream. For $0.1 < St_{\text{swirl}} < 1$ the drag force is not clearly dominant and the droplet will be centrifuged out of the swirling flow streamlines sooner or later. If the St_{swirl} is very large, i.e. $St_{\text{swirl}} > 1$, then the droplet is too heavy to respond to the airflow movement and will be centrifuged across the fluid streamlines. Estimating the angular gas velocity, ω, from $\omega = W/r$, the calculated St_{swirl}-value for the present study falls in the range from 0.09 to 0.006 for droplet diameter equal to 4.5 μm (Fig. 7). The implication is that the measured values of the U, V and W in the size class 0–4.5 μm are adequate approximations to the gas velocity.

Fig. 8 displays the comparison between the two-phase three mean velocity components and shows that the droplets follow the gas perfectly only directly downstream of the nozzle exit where the smaller droplets are concentrated. Examination of the radial profile of mean gas axial velocity in Fig. 8a reveals a well-pronounced central recirculation zone, characterized by

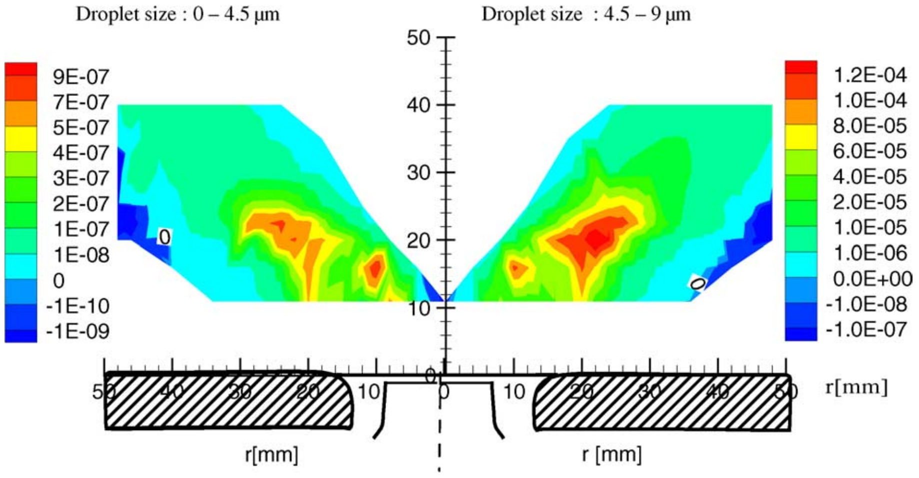

Fig. 6. Spatial distribution of the axial volume liquid flux (cm^3/cm^2 s).

Table 1
PDA measurements at $z = 11$ mm for $r = 2$ mm

Droplet size (μm)	Liquid flux (cm^3/cm^2 s)	Axial velocity (m/s)
0–4.5	-5.43×10^{-11}	−12.081
4.5–9	-2.20×10^{-9}	−16.840
9–13.5	$+2.94 \times 10^{-9}$	+15.80
13.5–18	$+1.74 \times 10^{-8}$	+10.87
18–22.5	$+4.72 \times 10^{-8}$	+19.79
22.5–27	0	

Volume diameter: 15.27 μm; Sauter mean diameter: 20.76 μm; mean axial velocity: −4.853 m/s; mean volume liquid flux: $+6.53 \times 10^{-8}$ cm^3/cm^2 s.

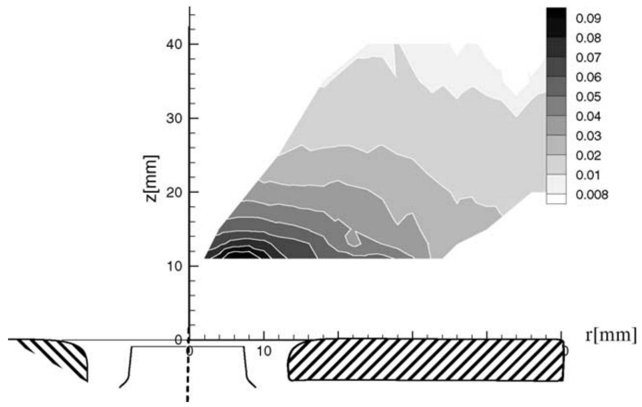

Fig. 7. Swirl Stokes number distribution for droplet size 4.5 μm.

negative values of this component closed to the centre line. It is interesting to observe that in the corner at the near-wall region the values of U are negative for the gas (depicting the CRZ), but positive for the droplets. This implies the droplets are incapable of following the gas movement and consequently penetrating the CRZ. At all measurement planes the results show that for both phases the mean axial velocity increases with the radial distance to reach a maximum value and then decreases toward the outer edge of the spray. As the flow diverges downstream, this maximum decreases. However, the result that catches the eye is that the droplets mean axial velocity component is found to be higher than that of the gas. This difference is more pronounced further downstream as well as in the CRZ (predominance of large droplets) due to the fact that droplets with negative velocity are not measured because they evaporate completely since they would have longer residence time inside the CRZ. In these areas the droplets cannot follow the local gas velocity profile and as a result the droplets “overshoot” the gas and the spray phase acts as a momentum source for the gas phase.

Generally, all profiles of the mean radial velocity show the typical behaviour of jets, i.e., linearity with radial distance in the centre region, followed by a decrease in the outer periphery (Fig. 8b). They reveal that there exists an inward motion of the droplets just downstream of the nozzle opening within the CTRZ. The radial velocity values are found to be close to those of the axial velocity, signifying large spreading in the radial direction. Therefore, the droplets cross the gas separation streamline as in liquid spray burning in the wake of a stabiliser disk [22]. It may be observed that the droplets exhibit a radial velocity larger than the gas in the inner and outer regions. The consequence is that the mean trajectory of the droplets is more steeply inclined outwards from the centreline than that of the gas. In the shear layer of the gas jet, the situation is reversed because of the fuel vapour addition and heat release from the flame, which cause an acceleration of the gas through their effects on the gas density. Further downstream, spreading of the jet and momentum loss to the droplets cause the gas to decelerate.

The radial profiles of the mean tangential velocity component for the liquid phase show trends similar to those of the gas (Fig. 8c). It consists at the nozzle exit of the combined forced-free vortex. It should be noted

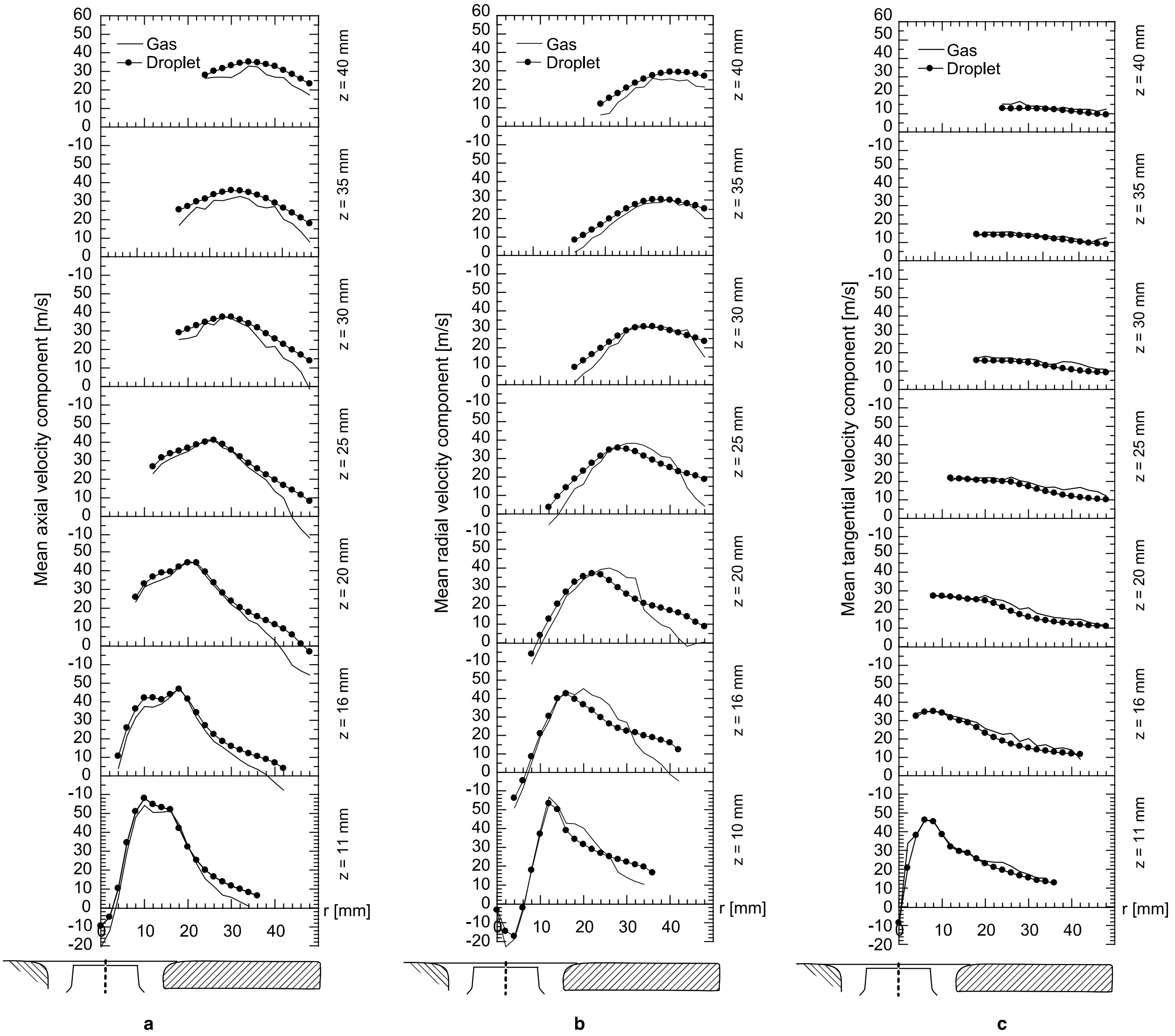

Fig. 8. (a) Axial velocity component radial profiles at various axial stations, (b) radial velocity component radial profiles, and (c) tangential velocity component radial profiles at various axial stations.

that at all positions, the droplets mean tangential velocity lags behind the gas one since the droplets (being large) have low velocities due their higher inertias. With growing axial distance, the tangential mean velocity decreases substantially in the central region, without any change in the periphery of the spray. Further downstream, the effect of inlet conditions (Rankine vortex structure) vanishes and the profile becomes uniform. The non-zero values recorded near the axis may arise from a residual alignment error or some instability of the central vortex location, as suggested by the higher turbulent kinetic energy values measured on the axis.

So far, the discussion has focused on the response of the droplet movement to the swirling gas flow. The concept can be extend to relate the turbulent response of the droplets to the turbulent motion of the gas through a turbulent Stokes number, St_{turb}, that characterizes the filtering affected by the inertia [23]:

$$St_{\mathrm{turb}} = \frac{\tau_{\mathrm{relax}}}{\tau_{\mathrm{turb}}} \tag{3}$$

An estimate of the time scale of the gas turbulence, τ_{turb}, can be based on a ratio of a turbulence length scale, l_{turb} and the square-root of the turbulent kinetic energy of the gas, k [23]:

$$\tau_{\mathrm{turb}} \approx l_{\mathrm{turb}}/\sqrt{k} \tag{4}$$

Here, l_{turb}, is set as $1/\sqrt{e}$ of the radius of the burner throat and hence $l_{\mathrm{turb}} \approx 0.36D_{\mathrm{b}}$ [24].

Fig. 9 shows radial profiles of the turbulent kinetic energy, for both gas and liquid phases, which is calculated using all three components of the velocity variance. The profile of k for the gas displays a discrete maximum whose radial position is defined by the intense production of turbulence in the shear region at the outer boundary of the internal recirculation zone where the

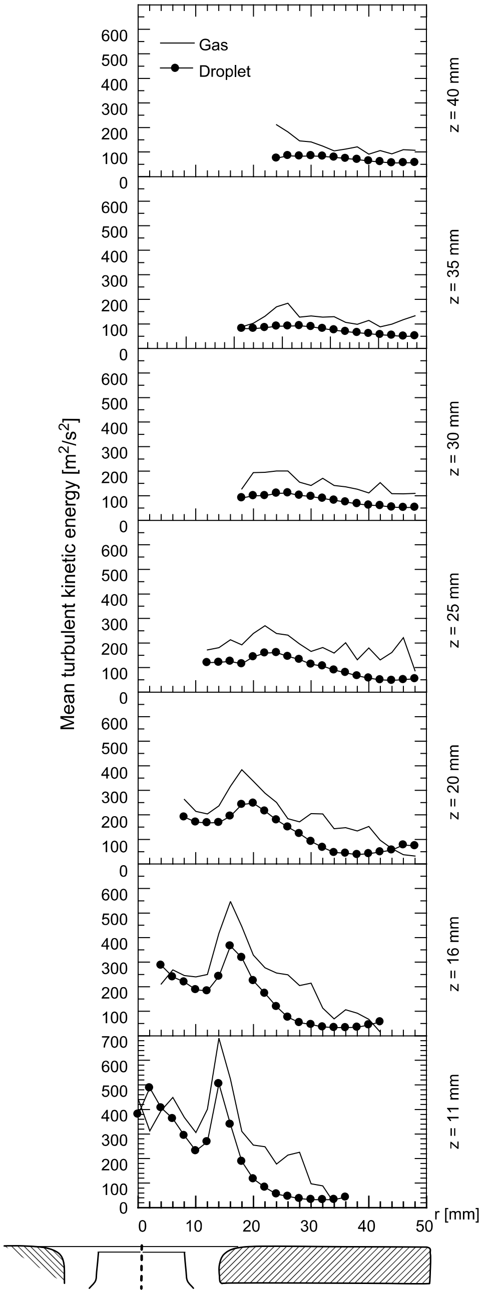

Fig. 9. Turbulent kinetic energy radial profiles at various axial stations.

respective gradients "$\partial U/\partial z$", "$\partial V/\partial r$" and "V/r" reach high values and hence dominate the turbulent generation rate, which is written in axisymmetric cylindrical coordinates as

$$P_k = \mu_t\left(2\left\{\left[\frac{\partial U}{\partial z}\right]^2 + \left[\frac{\partial V}{\partial r}\right]^2 + \left[\frac{V}{r}\right]^2\right\} + \left(\frac{\partial U}{\partial r} + \frac{\partial V}{\partial z}\right)^2 + \left(\frac{\partial W}{\partial z}\right)^2 + \left(\frac{\partial W}{\partial r} - \frac{W}{r}\right)^2\right) \tag{5}$$

The "$\partial U/\partial r$" and "$\partial V/\partial z$" terms were found in a separate investigation [25] to have the same order of magnitude but opposite contributions, which nullifies the effect of their sum on P_k. The last two terms in Eq. (5) could be neglected without incurring any significant error as their magnitudes are considerably smaller when compared to the other terms. Farther downstream, the turbulence level begins to decay owing to the diffusion toward to the outer shear of the turbulent kinetic energy and to its transfer to droplets. In particular, this attenuation is significant in the shear layer because of the additional dissipation introduced by the presence of droplets, which increases with St_{turb} and the droplet number density [26]. At a height of $z = 30$ mm, the peak disappears and the profile of k becomes almost uniform.

The turbulent kinetic energy of the droplets follows the same trend as that of the gas. However, the most noticeable difference is that the droplet turbulent kinetic energy is everywhere smaller than the gas one. This is evident as the droplets are large and the calculations of St_{turb} suggest that only droplets smaller than 25 μm can be affected by the large turbulent eddies of the gas flow. It may then be deduced that the gain in the turbulent kinetic energy (no decrease in spite of the diffusion) for the droplets is mainly due to the "fan spreading" phenomena [27]. Here, given the high value of St_{turb} for the droplets in this region, turbulence cannot be transferred from the air to them, and hence the turbulent kinetic energy of the droplets is generated by the superposition of droplet ($St_{\text{turb}} < 1$) trajectories from different regions of the flow. Similar results are obtained in a numerical simulation [28], where the Eulerian/Lagrangian approach was used to study the particle dispersion within turbulent shear flows.

Fig. 10 (right side) displays a flow field of droplets as a vector plot overlaid on the SMD. Every vector represents the sum of the local axial and radial velocity components at all measured positions. This figure clearly shows the limit of an internal recirculation zone with a very small amount of liquid fuel and a dispersion of droplets to the wall with large radial velocity.

3.5. Influence of air preheat

Since the desired performance requirements in terms of higher engine thrust/weight ratio and lower specific fuel consumption will call for higher turbine inlet temperatures, measurements were also conducted at an air preheat temperature of 400 °C with the same operating parameters. This implies that an increase in the air inlet temperature raises the gas velocity (consequently the droplets one) as it has been displayed in Fig. 10 (left side). Since the air of the swirled inner airflow has a large normal velocity component relative to the fuel film in the Venturi, the prompt atomization criterion applies here [29]. This process is assumed to occur if the airflow impacts on the liquid film at an appreciable angle. In this case, the interaction between the liquid and the

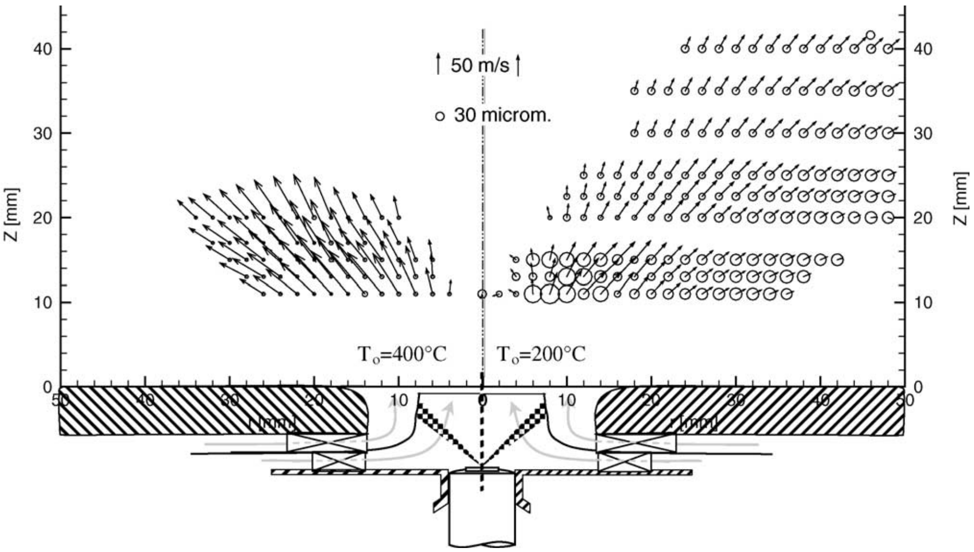

Fig. 10. SMD (μm) and vector velocity (U, V) distributions of droplets at air preheat temperature of 200 °C and 400 °C.

atomizing air is both strong and immediate. In consequence, the liquid sheet emerging from the nozzle has no time to build up the wavy structure but is violently torn into small fragments by the vigorous interaction created between the liquid and the colliding air jets. These fragments then contract into ligaments, which in turn fracture rapidly, forming droplets of various sizes in a time break-up defined by the following expression [30]:

$$t_{\mathrm{b}} = 5.0 d_{\mathrm{b}} \sqrt{\frac{\rho_{\mathrm{L}}}{\rho_{\mathrm{A}}}} \frac{1}{U_{\mathrm{A}}} \tag{6}$$

where d_{b} is the droplet size before the break-up process and U_{A} is the velocity of the atomizing airflow.

Under these conditions, the mean initial droplet size d_0 in the spray is controlled mainly by the ratio of the energy required for atomization, E_{L}, to the kinetic energy of the atomizing air, E_{A}. E_{L} is equal to the product of the liquid surface tension σ and the change in surface area (after and before atomization), i.e.

$$E_{\mathrm{L}} = \sigma\left(\frac{6\dot{m}_{\mathrm{L}}}{\rho_{\mathrm{L}} d_0} - \frac{2\dot{m}_{\mathrm{L}}}{\rho_{\mathrm{L}} t_{\mathrm{L}}}\right) \tag{7}$$

and E_{A} is given by

$$E_{\mathrm{A}} = \dot{m}_{\mathrm{A}} U_{\mathrm{A}}^2/2 \tag{8}$$

Equating the above energies, introducing a coefficient C to represent the efficiency of the atomization process and rearranging give the following expression for the mean initial droplet diameter:

$$d_0 = \frac{3}{\dfrac{1}{t_{\mathrm{L}}} + \dfrac{C\rho_{\mathrm{L}} U_{\mathrm{A}}^2}{4\sigma}\mathrm{AFR}} \tag{9}$$

where AFR denotes the air-to-fuel mass rate ratio, $\dot{m}_{\mathrm{A}}/\dot{m}_{\mathrm{L}}$. However, the assumption embodied by the term AFR in Eq. (9) that all of the air is equally effective in atomizing the liquid is not true in practice, where the addition of more atomizing air is less effective in reducing droplet size. To remedy to this problem, the AFR term in the semi-empirical expression for d_0 is replaced with the parameter $(1 + 1/\mathrm{AFR})^{-1}$. This substitution allows the influence of AFR on mean initial droplet size to diminish with an increase in AFR. By replacing d_0 with SMD_0, Eq. (9) becomes:

$$\mathrm{SMD}_0 = \frac{3}{\dfrac{1}{t_{\mathrm{L}}} + \dfrac{C'\rho_{\mathrm{L}} U_{\mathrm{A}}^2}{4\sigma(1 + 1/\mathrm{AFR})}} \tag{10}$$

Since experimental results confirm that initial liquid sheet thickness has only a minor influence on the droplet sizes produced in the spray [31], Eq. (10) indicates that, in this configuration and maintaining other parameters fixed, SMD_0 depends only on the velocity of the atomizing air. This is, in fact, precisely the result found in a full-scale aircraft airblast atomizer at subatmospheric conditions [32]; more specifically, that the kinetic energy of the air stream is the governing factor in the fuel atomization due to its effect on Weber number (We), which is the ratio of the disruptive aerodynamic forces to the surface tension cohesive forces. Thus, an increase in air preheat temperature raises the airflow velocity and hence reduces the SMD_0. Furthermore the temperature rise probably increases the initial fuel temperature at the prefilming lip. The surface tension of kerosene is reduced with increasing liquid temperature [33]. As the initial fuel temperature is unknown in this investigation, the change in surface tension is not taken into consideration. However, if it can be assumed that the difference of the air preheat is only felt by the fuel when in direct contact with the air and

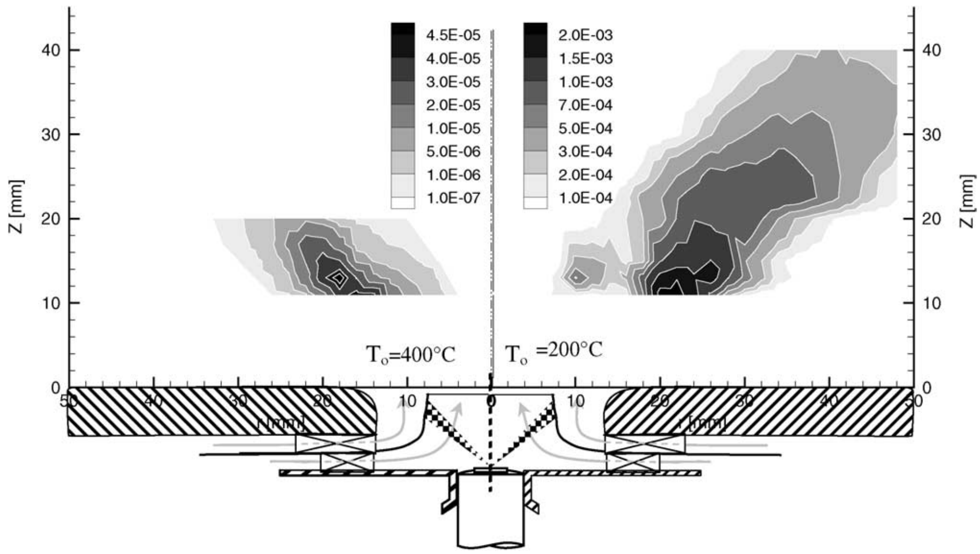

Fig. 11. Distribution of liquid volume flux (cm^3/cm^2 s) at air preheat temperature of 200 °C and 400 °C.

not only by a temperature difference of the injector itself, the heat-up is bound to be small, because the prefilming length is short (Fig. 1).

In addition, the influence of air velocity on mean droplet size may be manifested not solely through its effect on air momentum, but also through its effect on the break-up time. Thus from Eq. (6) and assuming the liquid density and the air mass flow rate are constant, one sees that t_b is inversely proportional to the square root of the atomizing airflow velocity, i.e. $t_b \propto 1/\sqrt{U_A}$. Hence, with increase air velocity, the ligament sheets disintegrate earlier, resulting in shorter break-up lengths and smaller droplets.

On the other hand, it is evident that air preheat temperature affects the evaporation process of droplets assuming to be described by the so-called d_0^2-*law*:

$$d^2(t) = d_0^2 - Kt \tag{11}$$

where K is known as the evaporation constant which increases markedly with an increase in surrounding temperature. Thus, the intense evaporation with higher preheated air temperature causes smaller droplets to disappear faster and gives rise to large droplets. Unfortunately, this influence did not appear to affect the droplet size in this study because it is dominated by the opposite effect (reduction in initial droplet size) created by the increase of the incoming airflow velocity.

It is found from Figs. 10 and 11 that both the axial penetration and radial dispersion decrease with an increase in inlet air temperature. This is because of the higher drag force per unit mass for droplets having lower SMD-value. Hence the fuel droplets with smaller SMD tend to regroup, vaporize locally and form an effective vapour mixture within the shear layer, thus the combustion is more concentrated inside a smaller. It then leads to higher temperature, correspondingly a higher level of NO_x emissions.

4. Conclusion

The phase-Doppler anemometry technique was used in this investigation and provided useful information on the characteristics of a kerosene spray flame from an airblast atomizer, which has not been studied in detail before, and which is typical for gas turbine applications. The measured flux distributions were representative of a hollow cone spray and close to the distributions of droplet number density.

The velocity measurements were conditionally processed in order to separate the data obtained from large particles (representing the liquid phase) and very small particles (representing the motion of the gas phase). They have put in evidence the existence of a central and a corner recirculation zones. The droplets were concentrated in the shear layer with highest turbulence activity. Additionally, the results reveal that the gas turbulent kinetic energy is at each location higher than the droplet one, and a small amount of liquid fuel characterized by a few smaller droplets has been found in the centre of the combustion chamber. These observations, which have undesirable implications in the context of the flame stabilization and the combustion efficiency, stem from the size dependent ability of droplets to follow the airflow, avoid the high centrifuging due to swirl, and to be affected by the turbulent characteristics of the gas flow. Hence, the mixing field of air with spray flame differs from that of gaseous fuel flame at identical operating conditions and an optimum droplet size for this burner configuration may be around 20–30 μm.

The measured decrease in droplet size with the increase of the air preheat temperature while keeping the fuel and air mass rates constant is caused by the increase in the atomizing airflow velocity which forms smaller initial droplets, follow by the increase of the evaporation rate.

Finally the results obtained can help in understanding the complex mixing process between fuel and air which takes place in industrial burners. They also provide useful information, which may be applied in the optimisation of the design of burners and their operating conditions, aiming to improve combustion efficiency and control exhaust gases.

Acknowledgement

The authors gratefully acknowledge the financial support of the BMBF for funding during the KEROMIX program and of the DAAD for the award of a fellowship to R. Hadef.

References

[1] R. Sellens, W. Zeng, Modeling spectral influences in droplet/turbulence interaction, in: ILASS Americas, 11th Annual Conference on Liquid Atomization and Spray Systems, Sacramento, CA, May 1998.

[2] W.D. Bachalo, M.J. Houser, Phase-Doppler spray analyser for simultaneous measurements of drop size and velocity distributions, Optical Engineering 235 (1984) 583–590.

[3] A.H. Lefebvre, D. Miller, The development of an airblast atomizer for gas turbine application, COA-Report-Aero-193, College of Aeronautics, Cranfield, England, 1996

[4] I.S. Carvalho, M.V. Heitor, The break-up of a annular liquid sheet downstream of an airblast prefilming atomizer, in: 10th Symposium on Turbulent Shear Flows, Pennsylvania State University, University Park, PA, 1995, pp. 3.97–3.102.

[5] A.K. Gupta, D.G. Lilley, N. Syred, Swirl Flows, Abacus Press, 1984.

[6] K. Merkle, A. Ament, B. Lenze, W. Leuckel, R. Hadef, Untersuchungen zum stabilitätsverhalten einer air-blast Zertäuberdüse, VDI Berichte 1492 (1999) 449–459.

[7] Y. Hardalupas, A.M.K.P. Taylor, J.H. Whitelaw, Velocity and size characteristics of swirling liquid-fuelled flames, Proceedings of the Royal Society of London Series A 428 (1990) 129–155.

[8] A.W. Marshall, A.K. Gupta, Effects of jet momentum distribution on thermal characteristics of co-swirling flames, Paper No. 9, 34th AIAA Aerospace Sciences Meeting, 1996, Reston, VA.

[9] A. Ateshkadi, V.G. Mc Donell, G.S. Samuelsen, Effect of hardware geometry on gas and drop behaviour in a radial mixer spray, in: 27th Symposium (International) on Combustion, 1998, pp. 1985–1992.

[10] R. Hadef, K. Merkle, B. Lenze, W. Leuckel, An experimental study of airblast atomizer spray flames, Journal of Energy 73 (2000) 50–55.

[11] A.H. Lefebvre, Atomization and Sprays, Hemisphere Publishing Corp., New York, 1989.

[12] H.-E Albrecht, M. Borys, N. Damaschke, C. Tropea, Laser Doppler and Phase Doppler Measurement Techniques, Springer-Verlag, Heidelberg, 2003.

[13] C. Tropea, T.-H. Xu, G. Grehan, F. Onofri, G. Gréhan, P. Haugen, M. Stieglmeier, Dual-mode phase-Doppler anemometry, Particle and Particle Systems Characterization 13 (1996) 165–170.

[14] K. Dullenkopf, M. Willmann, S. Wittig, F. Schöne, M. Stieglmeier, C. Tropea, Chr. Mundo, Comparative mass flux measurements in sprays using patternator and phase-Doppler technique, Particle and Particle System Characterisation 15–2 (1998) 84–89.

[15] M. Willmann, L. Eigenmann, S. Wittig, E.D. Hirleman, Experimental investigations on the effects of trajectory dependent scattering on PDA sizing with a standard instrument, in: 7th International Symposium on Applications of Laser Techniques to Fluid Mechanics, July 20–23, 1994, pp. 18.1.1–18.1.8.

[16] F. Durst, C. Tropea, T.-H. Xu, The slit effect in the phase Doppler anemometry, in: 2nd International Conference on Fluid Dynamic Measurement and Applications, Beijing, China, October 19–22, 1994, pp. 38–43.

[17] N. Damaschke, G. Gouesbet, G. Grehan, H. Mignon, C. Tropea, Response of PDA systems to non-spheroidal droplets, in: 13th Annual Conference on Liquid Atomization and Spray Systems, Florence, Italy, 1997, pp. 382–388.

[18] M. Saffman, Automatic calibration of measurement volume size, Applied Optics 26 (1987) 2592–2597.

[19] W. Leuckel, Swirl Intensities, Swirl types and energy losses of different swirl generating devices, IFRF-Doc. No. G02/a/16, Ijmuiden, 1967.

[20] Zh. Zhang, S. Ziada, PDA measurements of droplet size and mass flux in the three-dimensional atomisation region of water jet in air cross-flow, Experiments in Fluids 28 (2000) 29–35.

[21] R.P. Dring, M. Suo, Particle trajectories in swirling flows, Journal of Energy 2 (1978) 232–237.

[22] C.G. McCreath, N.A. Chigier, Liquid-spray burning in the wake of a stabilized disc, in: 14th Symposium (International) on Combustion, 1973, pp. 1353–1363.

[23] C. Hassa, Experimentelle Untersuchung der Turbulenten Partikeldispersion in Drallströmungen, DLR Forschungsbericht 20 (1994).

[24] H.J. Tennekes, L. Lumley, A First Course in Turbulence, MIT Press, Cambridge, MA, 1972.

[25] K. Merkle, H. Haessler, H. Büchner, N. Zarzalis, Effect of co- and counter-swirl on the isothermal flow- and mixture-field of airblast atomizer nozzle, International Journal of Heat and Fluid Flow 24 (2003) 529–537.

[26] X. Yang, N.H. Thomas, L.J. Guo, Particle dispersion in organized vortex structures within turbulent free shear flows, Chemical Engineering Science 55 (7) (2000) 1305–1324.

[27] Y. Hardalupas, A.M.K.P. Taylor, J.H. Whitelaw, Velocity and particle flux characteristics of turbulent particle-laden jets, Proceedings of the Royal Society of London Series A 426 (1989) 31–78.

[28] X.-Q. Chen, Heavy particle dispersion in inhomogeneous, anisotropic, turbulent flows, International Journal of Multiphase Flow 26 (2000) 631–635.

[29] A.H. Lefebvre, Energy considerations in twin-fluid atomization, Journal Engineering Gas Turbines Power 114 (1992) 89–96.

[30] P.-K. Wu, L.-P. Hsiang, G.M. Faeth, Aerodynamic effects on primary and secondary break-up, in: Liquid Rocket Engine Combustion Instability, in: V. Yang, W. Anderson (Eds.), Progress in Astronautics and Aeronautics, Vol. 169, AIAA, Washington, DC, 1995, pp. 247–279.

[31] N.K. Rizk, A.H. Lefebvre, Influence of liquid film thickness on airblast atomization, ASME Journal of Engineering for Power 102 (1980) 706–710.

[32] B.N. Caines, R.A. Hicks, C.W. Wilson, Influence of sub-atmospheric conditions on the performance of an airblast atomizer, AIAA Paper, 2001, pp. 2001–3573.

[33] M. Rachner, Die Stoffeigenschaften von Kerosin Jet A-1, in: Mitteilung 98-01, Institut für Antriebstechnik (Köln), Deutsches Zentrum für Luft- und Raumfahrt, ISSN 1434-8462, 1998.